Feature-driven topology optimization method preserving component sequences considering turning angle constraint

Dongsheng Jia[1,2*], Lei Liu[2], Jihong Zhu[2], Yu Zhang[1,2*], and Vassili Toropov[1]

[1] *School of Engineering and Material Science, Queen Marry University of London, London, E1 4NS, UK;*

[2] *State IJR Center of Aerospace Design and Additive Manufacturing, Northwestern Polytechnical University, Xi'an 710072, China*

Component sequence preservation is an intrinsic requirement in typical engineering applications, such as deployable chain-like structures, 3D printing structures with contour-parallel toolpaths, additive manufacturing of continuous fibre-reinforced polymer structures, customized stents, and soft robotics parts. This study presents a feature-driven method that preserves component sequences accounting for engineering requirements. The chain-of-bars design variables setting scheme is developed to realize the sequential component's layout, which sets the current bar's end point as the next bar's start point. The total length of the printing path is constrained to reduce the consumption of material accurately. Also, the angle between adjacent bars is constrained to avoid sharp angles at the turning point of the 3D printing path. Next, the sensitivity analysis considering the inter-dependence of substructures is performed. Several numerical examples are given to demonstrate the validity and merits of the proposed method in designing structures preserving component sequences.

Topology optimization, Component sequence preservation, Chain-like structures, Feature-driven method, Additive manufacturing

1. Introduction

The component sequence preservation of a structure means that the structural members are sequentially connected from the start point to the end point. Such a technique is needed in several engineering applications, such as self-folding structures [1], 3D printing structures with contour-parallel toolpaths [2], additive manufacturing of continuous fibre-reinforced polymer (AM-CFRP) structures [3-6], customized stents [7], and soft robotics [8]. For example, a deployable chain-of-bars structure is folded in the launcher acting as a supporting structure, and deployed in orbit acting as the frame structures of a solar energy panel. In order to realise these multi-functions [9-13], the deployable chain-of-bars structure is manufactured by the 5-axis 3D printer

[14-17] with morphable material [18]. Another typical example is AM-CFRP structures, the continuous carbon fibre filament with high specific strength and resins filament with lower strength are co-extruded from the 3D printing nozzle in a line to form a complete structure consisting of a chain of bars [4,6]. For the optimization of chain-of-bars structures, engineering requirements, such as the turning angle of the 3D printing toolpath, should be considered [19-21]. The turning angle of the 3D printing toolpath is significantly important for manufacturing quality because the material deposition along the toolpath with a sharp corner leads to a bulge at the corner, as shown in Fig. 1a [22]. The over-extrusion comes from the fact the liquefier continues to extrude material while the speed of the printing head is unavoidably reduced when approaching the sharp corner. Also, sharp turns generate inconsistent printing widths, as shown in Fig. 1b. This results in underfilling regions (porous surfaces) where the printed material cannot reach, correspondingly, the loss of stiffness. Sharp corners can also re-
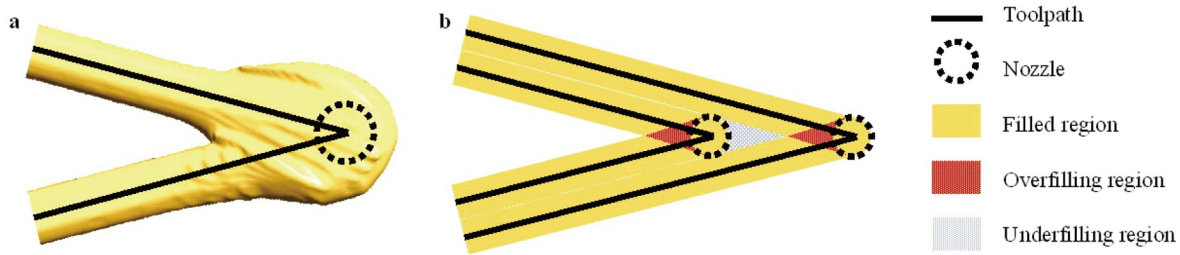
Figure 1 Problems at sharp corner. **a** A simulation result of a bulge at the single-path sharp corner [22]. **b** Schematic of underfilling and overfilling region at the parallel-path sharp corner.

sult in overfilling areas where the material is printed twice, causing the build-up of pressure in the nozzle system and bulges on the surface [2]. Thus, control of the minimum size of the angle of the toolpath in the 3D printing of the chain-of-bars structure is necessary for structural topology optimization.

Topology optimization is an advanced design method to obtain innovative structural configurations. It effectively finds the optimum material layout within a predefined design domain [23,24]. A variety of topology optimization methods have been proposed for decades, including the homogenization method [25], the density method [26-37], the evolutionary structural optimization (ESO) method [38-40], and the level set method [41-46]. Recent reviews of research developments and engineering applications of topology optimization include papers [5,47,48]. However, those typical topology optimization methods cannot be used for preserving the component sequence since there is no explicit information on the geometry of the topology model. For example, the density method relates the structural topology to the finite element model rather than a feature-based geometry model. In order to describe the geometry features in structure, a feature-driven topology optimization method [49-56] has been proposed in recent years. This method originated from the multi-component design method [57], where components are used as parts of a load-bearing path. In the feature-driven method, a structure is considered as an assembly of multiple geometric features and components. The components can be defined using key parameters, such as length, width, rotation angles, central points, endpoints, and other geometry features, which are necessary for engineering applications. Structural topology optimization is realized via components' shape and position optimization. Various geometric features have been proposed, including super-ellipse, closed B-spline, and bar with semi-circular ends [58,59]. One of the merits of the feature-driven method is that the geometric characteristics of the component are explicitly expressed so that the engineering constraints can be controlled conveniently by the geometric characteristics of the component. For example, the polygon features are used as basic design primitives that establish a self-supporting structure design for additive manufacturing [60].

The void-free structures are designed by setting the centre of the super-ellipse and closed B-spline outside the design domain [59].

These topology optimization methods have not been applied to the design of chain-of-bars structures, and therefore have not applied controls to the minimum size requirements of the turning angle of the toolpath nor to the interdependent relationships among structural components. In this work, a feature-driven method preserving the component sequence is developed to optimize chain-like structures. In this method, the inter-dependence of sub-structures is analytically controlled by the initial design variables setting scheme, the constraint on the angle between adjacent components and the total length of the components. A bar with semi-circular ends is used as a basic design feature. The sequential layout of components is ensured by setting the current bar's end point as the next bar's start point. The positions of the bar's end points are regarded as design variables and the width is kept constant. Furthermore, a constraint on the angle between adjacent bars is introduced to avoid the sharp angle problem.

This study is organized as follows. In Sect. 2, a feature-driven topology optimization method preserving the component sequence for a chain-like structure is introduced. The chain-of-bars design variables setting scheme is proposed. Angle constraints between adjacent bars and total length constraints are introduced. In Sect. 3, a mathematical formulation of this optimization problem is provided, and sensitivity analysis for compliance, total length, and angle constraints of chain-like structure is presented. In Sect. 4, three numerical examples are provided to illustrate the validity of the proposed optimization method. In Sect. 5, conclusions are presented.

2. Feature-driven topology optimization method preserving component sequences

This section presents a feature-driven topology optimization method considering the inter-dependence of sub-structures due to requirements of manufacturing in sequence. First, the chain-of-bars design variables setting scheme is introduced.

Next, the geometry description of the bar using the level set function (LSF) is presented, and the total length constraint is defined. Finally, angle constraints between adjacent bars are added.

2.1 Chain-of-bars design variables setting scheme

Many engineering structures consist of components in sequence to satisfy manufacturing requirements. However, typical density-based topology optimization methods cannot handle the required component features and the inter-dependence of substructures. Although a recently introduced feature-driven method has been used to describe the geometry of moving components in several design variables, the moving components in this method are considered independent. Suppose the inter-dependence of moving components needs to be considered while using the original feature-driven method, as shown in Fig. 1a. In that case, many additional constraints must be imposed to connect two adjacent endpoints.

The chain-of-bars design variables setting scheme is demonstrated in Fig. 2b, where the bars are connected end-to-end as a chain. The coordinates of each end node (x_i, y_i) ($i = 1, 2, \ldots, N_{\text{node}}$) of bar Φ_i ($i = 1, 2, \ldots, N_{\text{bar}}$) in the chain are chosen as design variables for designing the chain-like structure. The angles between two adjacent bars are defined as β_i ($i = 1, 2, \ldots, N_{\text{angle}}$). The key parameters of the chain-like structure are listed in Table 1, where the relationship among N_{node}, N_{bar}, and N_{angle} can be defined as $N_{\text{bar}} = N_{\text{node}} - 1$
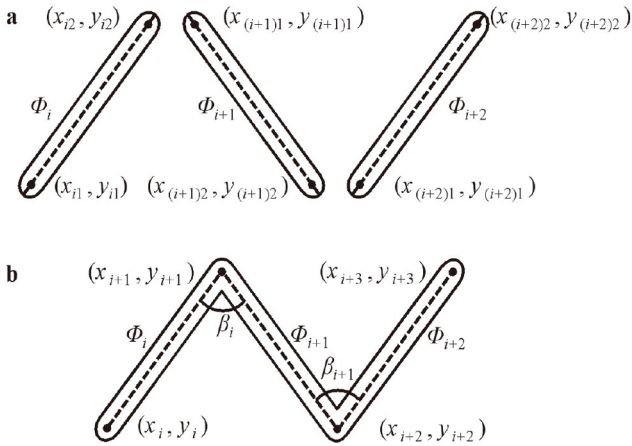

Figure 2 Schematic of design variables setting scheme. **a** Design variables setting scheme in the original feature-driven method. **b** The chain-of-bars design variables setting scheme and the angles between adjacent bars.

Table 1 Key parameters of the chain-like structure

Parameters	Notation	Range
Angles between adjacent bars	β_i	$i = 1, 2, \ldots, N_{\text{angle}}$
LSF of individual bar	Φ_i	$i = 1, 2, \ldots, N_{\text{bar}}$
End nodes of bars	(x_i, y_i)	$i = 1, 2, \ldots, N_{\text{node}}$

and $N_{\text{angle}} = N_{\text{node}} - 2$. The chain-of-bars design variables setting scheme is more efficient than the original feature-driven method for building a structural topological optimization model preserving component sequence. For example, if the number of bars is N_{bar}, in order to connect two adjacent endpoints, it needs to introduce $4N_{\text{bar}}$ design variables and $N_{\text{bar}} - 1$ additional constraints in the original feature-driven method. In comparison, the method with a chain-of-bars design variables setting scheme can solve these problems with only $2(N_{\text{bar}} + 1)$ design variables and no additional constraints.

2.2 Parameterization using a bar with semi-circular ends

A 3D LSF can implicitly describe crisp 2D contours because it has continuous derivatives. It is crucial because a crisp description of structure shape benefits the treatment of changes in the topology optimization process. In this study, the 2D contour of the moving bar is parameterized by a 3D LSF of a bar consisting of a rectangular cross-section and semi-circular ends.

For the two-phase (solid and void) material problem, the LSF Φ_i is described as

$$\begin{cases} \Phi_i(\mathbf{X}) > c \iff \mathbf{X} \in \Omega, \\ \Phi_i(\mathbf{X}) = c \iff \mathbf{X} \in \Gamma, \\ \Phi_i(\mathbf{X}) < c \iff \mathbf{X} \in \Lambda, \end{cases} \tag{1}$$

where Ω represents the material domain, Λ represents the void domain, Γ means the solid-void interface, c is a constant usually set as 0, and $\mathbf{X}$ is a point within the design domain. The division of the material domain is shown in Fig. 3a. The fixed grid finite element method [61] is used to discretize the structure with a solid-void interface described by continuous LSF.

Figure 3b and c depict the LSF of a bar with semi-circular ends and the corresponding parameterization of geometric features. The width of bars $D = 2r$ is set as a constant value. Therefore, the coordinates of the centers of semi-circular ends are adopted as design variables $\{x_i, y_i, x_{i+1}, y_{i+1}\}$ in a corresponding LSF to parameterize a bar. The LSF for the ith bar with semi-circular ends used herein employs the function Φ_i given by

$$\Phi_i = 0.5 - \frac{1}{1 + e^{-n(d_{e,i} - r)}}, \quad i = 1, 2, \cdots, N_{\text{node}} - 1, \tag{2}$$

where n is the adjustment factor ($n > 0$) controlling the width of the solid-void boundary band described by the LSF in Fig. 3b. In Eq. (2), $d_{e,i}$ is the distance from point E (a node within the range of variables of LSF) to bar i in Fig. 3c, which is given as
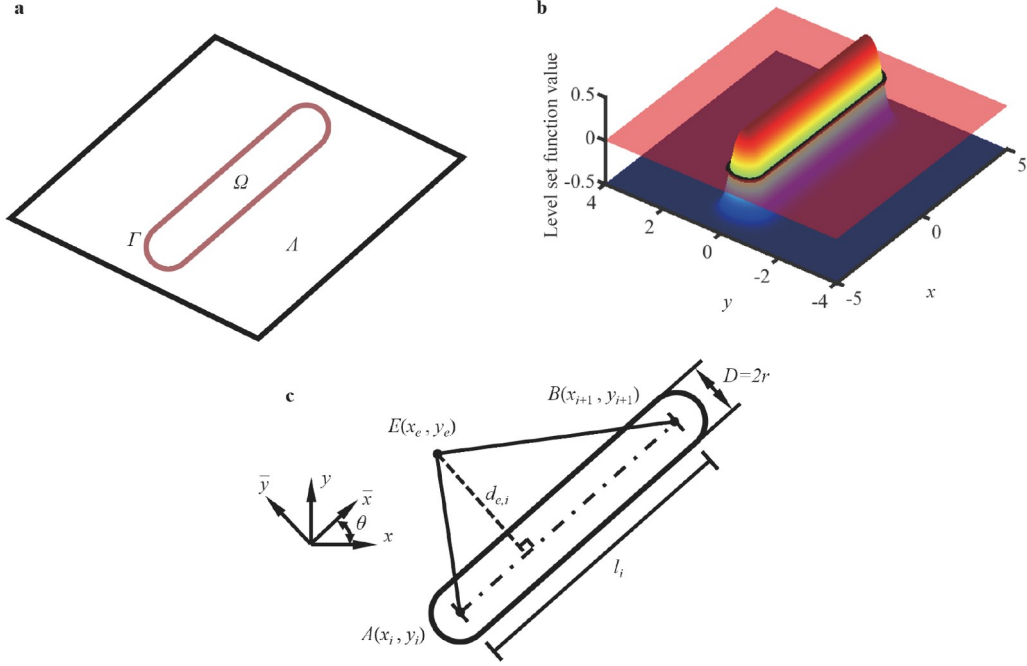
Figure 3 An example of a bar with semi-circular ends. **a** Division of the material domain. **b** The LSF. **c** The corresponding geometric parameterization.

$$d_{e,i} = \begin{cases} \sqrt{(\bar{x}_e - \bar{x}_i)^2 + (\bar{y}_e - \bar{y}_i)^2}, & \text{if } \bar{x}_e < \bar{x}_i, \\ \dfrac{\left\| \det |\mathbf{G}_{e,i}| \right\|}{l_i}, & \text{if } \bar{x}_i \leq \bar{x}_e \leq \bar{x}_{i+1}, \\ \sqrt{(\bar{x}_e - \bar{x}_{i+1})^2 + (\bar{y}_e - \bar{y}_{i+1})^2}, & \text{if } \bar{x}_e > \bar{x}_{i+1}. \end{cases} \quad (3)$$

In Eq. (3), $(\bar{x}_e, \bar{y}_e)$, $(\bar{x}_i, \bar{y}_i)$, and $(\bar{x}_{i+1}, \bar{y}_{i+1})$ are local coordinates on the moving bar. The subscript denotes the point E or centres of the bar ends (i or $i+1$), as shown in Fig. 3c. When $\bar{x}_e \in [-\infty, \bar{x}_i]$, $d_{e,i}$ is the distance from point E to point A, when $\bar{x}_e \in [\bar{x}_i, \bar{x}_{i+1}]$, $d_{e,i}$ is the distance from point E to the line $\mathbf{AB}$ which is calculated by $d_{e,i} = |\mathbf{AB} \times \mathbf{AP}|/|\mathbf{AB}| = \text{sign}\left(|\mathbf{G}_{e,i}|\right)|\mathbf{G}_{e,i}|/l_i$, when $\bar{x}_e \in [\bar{x}_{i+1}, +\infty]$, $d_{e,i}$ is the distance from point E to point B. $\mathbf{G}_{e,i}$ and l_i are defined as

$$\mathbf{G}_{e,i} = \begin{vmatrix} \bar{x}_e - \bar{x}_i & \bar{y}_e - \bar{y}_i \\ \bar{x}_{i+1} - \bar{x}_i & \bar{y}_{i+1} - \bar{y}_i \end{vmatrix}, \quad (4)$$

$$l_i = \sqrt{(x_{i+1} - x_i)^2 + (y_{i+1} - y_i)^2}. \quad (5)$$

The origin of local coordinates is the same as that of the global coordinate system. The local coordinates $(\bar{x}_\psi, \bar{y}_\psi)$ of points corresponding to moving bar i with semi-circular ends can be obtained from global coordinates (x_ψ, y_ψ) by rotating with respect to the z-axis

$$\begin{aligned} \bar{x}_\psi &= \cos\theta_i x_\psi + \sin\theta_i y_\psi, \\ \bar{y}_\psi &= -\sin\theta_i x_\psi + \cos\theta_i y_\psi, \end{aligned} \quad \psi = i, i+1, e, \quad (6)$$

described using the coordinate transformation matrix

$$\begin{vmatrix} \bar{x}_\psi \\ \bar{y}_\psi \end{vmatrix} = \begin{vmatrix} \cos\theta_i \sin\theta_i \\ -\sin\theta_i \cos\theta_i \end{vmatrix} \begin{vmatrix} x_\psi \\ y_\psi \end{vmatrix}, \quad (7)$$

with

$$\cos\theta_i = \frac{x_{i+1} - x_i}{l_i}, \quad \sin\theta_i = \frac{y_{i+1} - y_i}{l_i}. \quad (8)$$

To model the aggregation effect of all bars' LSF value on a point $(\bar{x}_e, \bar{y}_e)$, individual logistic terms in Eq. (2) can all be multiplied. Thus, the LSF of the whole chain-of-bars structure Φ is now expressed as

$$\Phi = 0.5 - \prod_{i=1}^{N_{\text{node}}-1} \frac{1}{1 + e^{-n(d_{e,i}-r)}}. \quad (9)$$

The total length of bars is introduced to control the consumption of printing materials and is defined as

$$L = \sum_{i=1}^{N_{\text{node}}-1} l_i. \quad (10)$$

2.3 Angle constraints of adjacent bars

After the chain-of-bars design variables setting scheme is adopted for the feature-driven topology optimization method, it is undesirable to have sharp angles between adjacent bars. Taking the schematic in Fig. 4a as an example, the 3D printing head moves in order from Point 1 (P_1) to Point 13 (P_{13}). The angle β_{10} between the adjacent bars 10 and 11 is nearly zero. Thus, the constraint of the angle between ad-
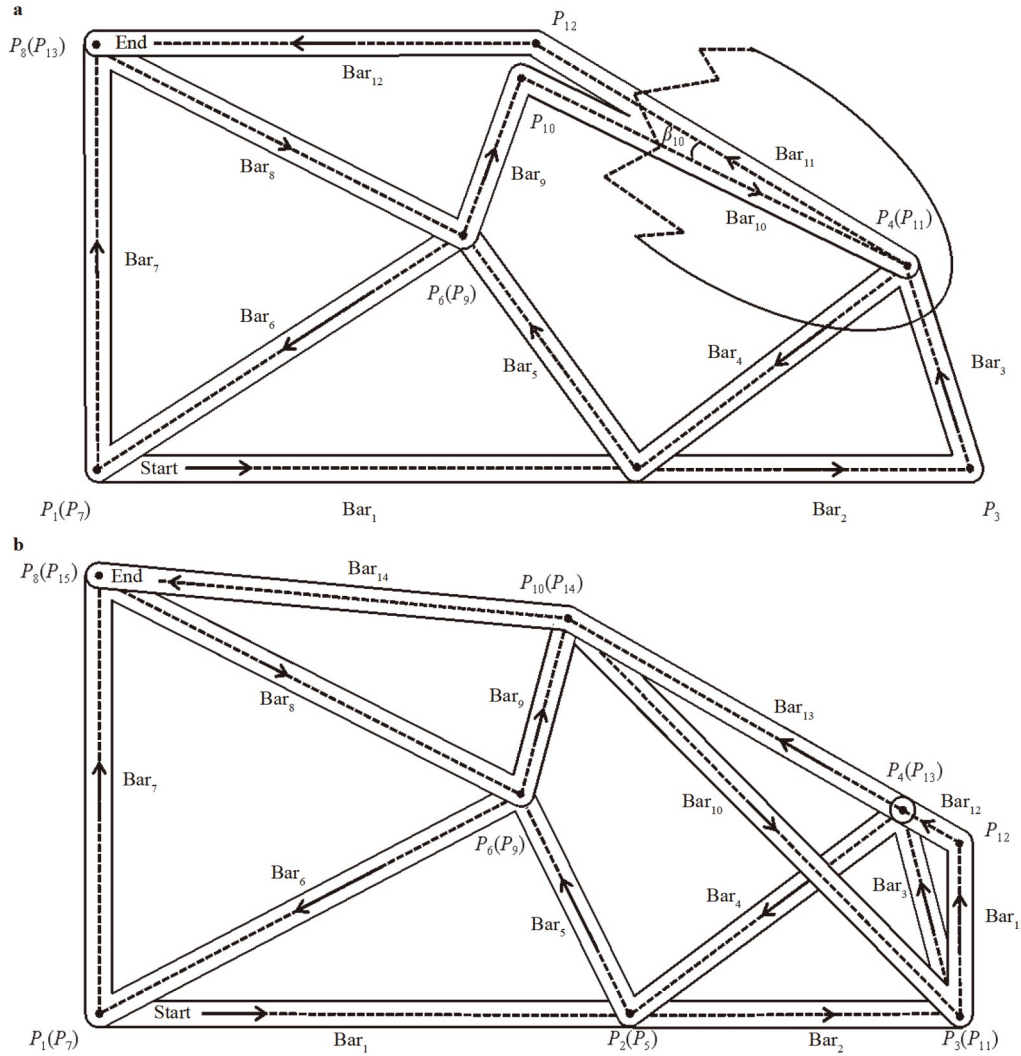
Figure 4 Schematic of sharp angle problems. **a** Result of optimization without constraints on angles between adjacent bars. **b** Result of optimization with constraints on angles between adjacent bars.

jacent bars is introduced to control the angle to a larger value.

The cosine of the angle between adjacent bars is introduced to constrain the angle and can be calculated as

$$f_i = \cos\beta_i = \frac{B_i}{l_i l_{i+1}}, i = 1, 2, \ldots, N_{node} - 2, \tag{11}$$

with

$$
\begin{aligned}
B_i &= (x_i - x_{i+1})(x_{i+2} - x_{i+1}) + (y_i - y_{i+1})(y_{i+2} - y_{i+1}), \\
l_i &= \sqrt{(x_{i+1} - x_i)^2 + (y_{i+1} - y_i)^2}, \\
l_{i+1} &= \sqrt{(x_{i+2} - x_{i+1})^2 + (y_{i+2} - y_{i+1})^2}.
\end{aligned}
\tag{12}
$$

$f_1, f_2, \ldots, f_i, \ldots, f_{Nangle}$ are aggregated into one formulation to replace the maximum function with the Kresselmeier-Steinhauser (KS) function [62]

$$A\left(f_1, f_2, \ldots, f_{N_{angle}}\right) = \frac{1}{p_{KS}} \ln\left(\sum_{i=1}^{N_{angle}} e^{p_{KS}(f_i - f_{max})}\right) + f_{max}, \tag{13}$$

where

$$f_{max} = \max\left(f_1, f_2, \ldots, f_{N_{angle}}\right). \tag{14}$$

p_{KS} is a positive integer to adjust the degree of approximation to the maximum function of f_i. For example, if the constraint on the angles among bars is in the range of $45° \leq \beta_i \leq 315°$, the function A can be set as $A \leq \sqrt{2}/2$. The schematic of the optimized result with angle constraints is shown in Fig. 4b, demonstrating that sharp angles do not appear.

When the boundary is a curved line, the internal point of straight bars may be located outside the boundary even though the two ends of straight bars are located within the boundary, as shown in Fig. 5. In order to prevent such cases, a constraint on the curved boundary is imposed.

The coordinates of an internal point on the straight bars can be calculated by
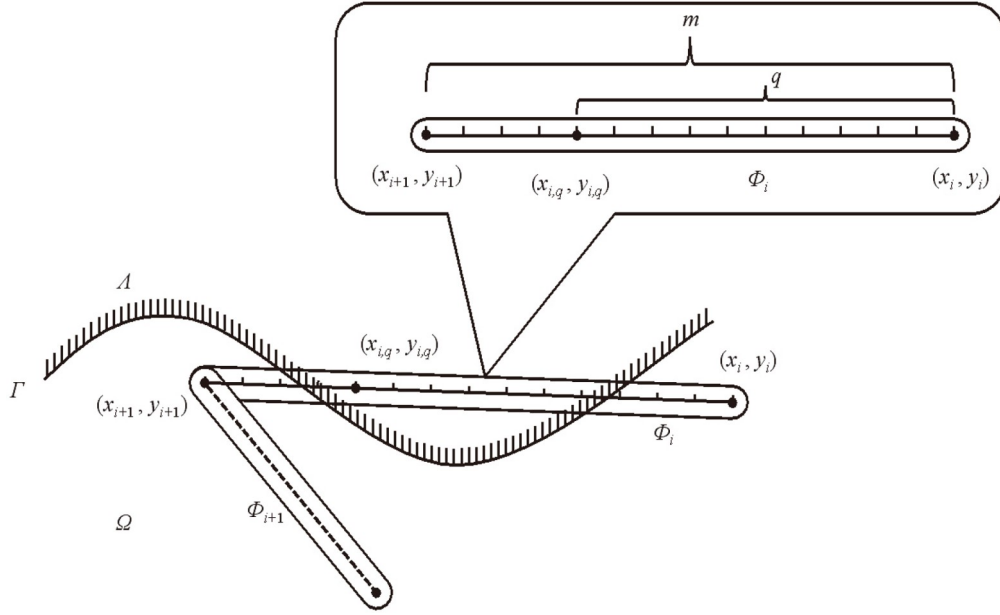
Figure 5 Schematic of curved boundary problems.

$$x_{i,q} = x_i + \frac{q}{m}(x_{i+1} - x_i),$$
$$y_{i,q} = y_i + \frac{q}{m}(y_{i+1} - y_i), \tag{15}$$
$$i = 1, 2, \cdots, N_{\text{node}} - 1, \quad q = 0, 1, \cdots, m,$$

where m is the number of divisions for the ith straight bar, and q is defined as the number of sub-divisions before the internal point $(x_{i,q}, y_{i,q})$.

For the convenience of calculation and derivation of functions, the LSF of the boundary curve is defined as

$$z = \sum_{k=0}^{8} a_k x^k - y. \tag{16}$$

The modified signed distance function [63] between an internal point and the boundary is defined as

$$z' = \frac{\sum\limits_{k=0}^{8} a_k x^k - y}{\sqrt{\left(\frac{\partial z}{\partial x}\right)^2 + \left(\frac{\partial z}{\partial y}\right)^2}}. \tag{17}$$

These distances for all bars can be aggregated into one differentiable function to approximately replace the minimum function with the KS function

$$\Delta = \frac{1}{p_{\text{KS}}} \ln\left[\sum_{i=1}^{N_{\text{node}}-1} \sum_{q=0}^{m} e^{p_{\text{KS}}(z' - z'_{\min})}\right] + z'_{\min}, \tag{18}$$

where p_{KS} is a negative number to adjust the degree of approximation to the minimum function,

$$z'_{\min} =$$
$$\min\left[z'(x_{1,1}, y_{1,1}), z'(x_{1,2}, y_{1,2}), \cdots, z'(x_{N_{\text{node}}-1,m}, y_{N_{\text{node}}-1,m})\right]. \tag{19}$$

For a case of curved boundary in Fig. 5, the moving bars can be limited to remaining inside the given domain by $\Delta \geqslant 0$.

3. The problem formulation and sensitivity analysis

3.1 Formulation of the topology optimization problem

This work aims to obtain the minimum compliance under specific boundary conditions satisfying constraints, including the total length constraint to limit the total material consumption and the minimum angle constraints on adjacent bars to avoid sharp angle problems in the manufacturing process. The mathematical formulation could be defined as

Find $\quad \xi = \{\mathbf{x}, \mathbf{y}\} = (x_1, x_2, ..., x_{N_{\text{node}}}, y_1, y_2, ..., y_{N_{\text{node}}}),$

Minimise $\quad C = \frac{1}{2} \int_{\Omega} E_{ijkl} \varepsilon_{ij}(u) \varepsilon_{kl}(u) H[\Phi(\xi)] \mathrm{d}\Omega,$

Subject to $\quad \begin{cases} \mathbf{KU} = \mathbf{F}, \\ VF = \int_{\Omega} H[\Phi(\xi)] \mathrm{d}\Omega / V_0 \leq \overline{VF}, \\ A \leq \overline{A}, \\ L \leq \overline{L}, \\ \Delta \geqslant 0, \\ X_{\min} \leq \mathbf{x} \leq X_{\max}, \\ Y_{\min} \leq \mathbf{y} \leq Y_{\max}, \end{cases} \tag{20}$

where C denotes the compliance, E_{ijkl} denotes the constitutive tensor of linear elasticity, ε_{ij} and ε_{kl} are strain tensors, VF is the volume fraction of the structure which is bounded by an upper limit $\overline{VF}$, V_0 is the volume of design

domain, L is the total length of the manufactured structure (defined in Eq. (10)) which is bounded by an upper limit $\overline{L}$, the vector of nodal coordinates ξ is the design variable that satisfies the curved boundary requirements $\Delta \geqslant 0$ and design domain $[X_{\min}, X_{\max}] \cap [Y_{\min}, Y_{\max}]$, the angle constraint function A (defined in Eq. (13)) is bounded by an upper limit $\overline{A}$, which means that the angles between adjacent bars are limited to $[\arccos \overline{A}, 2\pi - \arccos \overline{A}]$, the regularized Heaviside function $H(\Phi)$ is defined as

$$H(\Phi) = \begin{cases} 1, & \Phi \geqslant \eta, \\ \dfrac{3(1-\alpha)}{4}\left(\dfrac{\Phi}{\eta} - \dfrac{\Phi^3}{3\eta^3}\right) + \dfrac{1+\alpha}{2}, & -\eta < \Phi < \eta, \\ \alpha, & \Phi \leqslant -\eta, \end{cases} \quad (21)$$

where the parameter η is introduced for adjusting the accuracy of sensitivities, α is a small constant usually set as 0.001 [54].

3.2 Sensitivities analysis

3.2.1 Sensitivities analysis of compliance and volume fraction

The compliance C and volume fraction VF can be expressed as

$$\begin{aligned} C &= \frac{1}{2}\int_{\Omega} E_{ijkl}\varepsilon_{ij}(u)\varepsilon_{kl}(u)H[\Phi(\xi)]\mathrm{d}\Omega, \\ VF &= \int_{\Omega}\frac{H[\Phi(\xi)]\mathrm{d}\Omega}{V_0}, \end{aligned} \quad (22)$$

written in a general form

$$F(\Phi) = \int_{\Omega} f(x)H(\Phi)\mathrm{d}\Omega, \quad (23)$$

where Φ is the LSF (see Eq. (9)). The derivatives of $F(\Phi)$ with respect to design variables ξ are

$$\frac{\partial F(\Phi)}{\partial \xi} = \int_{\Omega} f(x)\frac{\partial H(\Phi)}{\partial \Phi}\frac{\partial \Phi}{\partial \xi}\mathrm{d}\Omega, \quad (24)$$

where the derivative of the modified Heaviside function is defined as $\partial H(\Phi)/\partial \Phi = 3/4(1-\alpha)(1/\eta - \Phi^2/\eta^3)$ in the interval $-\eta \leqslant \Phi < \eta$ and $\partial H(\Phi)/\partial \Phi = 0$ elsewhere [54].

The derivatives of LSF Φ with respect to design variables $\xi_i = x_i, y_i$ ($i = 1, 2, \cdots x_{N\text{node}}$) are

$$\frac{\partial \Phi}{\partial \xi_i} = \begin{cases} \dfrac{\partial \Phi}{\partial d_{e,i}}\dfrac{\partial d_{e,i}}{\partial \xi_i}, & \text{if } i = 1, \\ \dfrac{\partial \Phi}{\partial d_{e,i-1}}\dfrac{\partial d_{e,i-1}}{\partial \xi_i} + \dfrac{\partial \Phi}{\partial d_{e,i}}\dfrac{\partial d_{e,i}}{\partial \xi_i}, & \text{if } i = 2,3,\cdots,N_{\text{node}} - 1, \\ \dfrac{\partial \Phi}{\partial d_{e,i-1}}\dfrac{\partial d_{e,i-1}}{\partial \xi_i}, & \text{if } i = N_{\text{node}}, \end{cases} \quad (25)$$

where

$$\frac{\partial \Phi}{\partial d_{e,i}} = -(0.5 - \Phi)\frac{n\mathrm{e}^{-n(d_{e,i}-r)}}{1+\mathrm{e}^{-n(d_{e,i}-r)}}, \quad (26)$$
$$i = 1,2,...,N_{\text{node}} - 1.$$

$\partial d_{e,i}/\partial \xi_i$ can be calculated using the coordinate transformation matrix (see Eq. (7)) as

$$\begin{aligned} \frac{\partial d_{e,i}}{\partial \xi_i} &= \frac{\partial d_{e,i}}{\partial \overline{x}_i}\frac{\partial \overline{x}_i}{\partial \xi_i} + \frac{\partial d_{e,i}}{\partial \overline{y}_i}\frac{\partial \overline{y}_i}{\partial \xi_i} + \frac{\partial d_{e,i}}{\partial \overline{x}_{i+1}}\frac{\partial \overline{x}_{i+1}}{\partial \xi_i} \\ &\quad + \frac{\partial d_{e,i}}{\partial \overline{y}_{i+1}}\frac{\partial \overline{y}_{i+1}}{\partial \xi_i} + \frac{\partial d_{e,i}}{\partial \overline{x}_{e_i}}\frac{\partial \overline{x}_{e_i}}{\partial \xi_i} + \frac{\partial d_{e,i}}{\partial \overline{y}_{e_i}}\frac{\partial \overline{y}_{e_i}}{\partial \xi_i}. \end{aligned} \quad (27)$$

The derivatives $\partial d_{e,i}/\partial \overline{x}_i$, $\partial d_{e,i}/\partial \overline{y}_i$, $\partial d_{e,i-1}/\partial \overline{x}_i$, $\partial d_{e,i-1}/\partial \overline{y}_i$, $\partial d_{e,i}/\partial \overline{x}_e$, and $\partial d_{e,i}/\partial \overline{y}_e$ can be calculated as

$$\frac{\partial d_{e,i}}{\partial \overline{x}_i} = \begin{cases} \dfrac{(\overline{x}_i - \overline{x}_e)}{\sqrt{(\overline{x}_e - \overline{x}_i)^2 + (\overline{y}_e - \overline{y}_i)^2}}, & \text{if } \overline{x}_e < \overline{x}_i, \\ \text{sign}\left(|\mathbf{G}_{e,i}|\right)\left(\dfrac{\overline{y}_e - \overline{y}_{i+1}}{l_i} - \dfrac{\det|\mathbf{G}_{e,i}|}{l_i^2}\dfrac{\partial l_i}{\partial \overline{x}_i}\right), & \text{if } \overline{x}_i \leqslant \overline{x}_e \leqslant \overline{x}_{i+1}, \\ 0, & \text{if } \overline{x}_e > \overline{x}_{i+1}, \end{cases}$$
$$\frac{\partial d_{e,i}}{\partial \overline{y}_i} = \begin{cases} \dfrac{(\overline{y}_i - \overline{y}_e)}{\sqrt{(\overline{x}_e - \overline{x}_i)^2 + (\overline{y}_e - \overline{y}_i)^2}}, & \text{if } \overline{x}_e < \overline{x}_i, \\ \text{sign}\left(|\mathbf{G}_{e,i}|\right)\left(\dfrac{\overline{x}_{i+1} - \overline{x}_e}{l_i} - \dfrac{\det|\mathbf{G}_{e,i}|}{l_i^2}\dfrac{\partial l_i}{\partial \overline{y}_i}\right), & \text{if } \overline{x}_i \leqslant \overline{x}_e \leqslant \overline{x}_{i+1}, \\ 0, & \text{if } \overline{x}_e > \overline{x}_{i+1}, \end{cases} \quad (28)$$

$$\frac{\partial d_{e,i-1}}{\partial \overline{x}_i} = \begin{cases} 0, & \text{if } \overline{x}_e < \overline{x}_{i-1}, \\ \text{sign}\left(|\mathbf{G}_{e,i}|\right)\left(\dfrac{\overline{y}_{i-1} - \overline{y}_e}{l_i} - \dfrac{\det|\mathbf{G}_{e,i}|}{l_i^2}\dfrac{\partial l_{i-1}}{\partial \overline{x}_i}\right), & \text{if } \overline{x}_i \leqslant \overline{x}_e \leqslant \overline{x}_{i+1}, \\ \dfrac{(\overline{x}_i - \overline{x}_e)}{\sqrt{(\overline{x}_e - \overline{x}_i)^2 + (\overline{y}_e - \overline{y}_i)^2}}, & \text{if } \overline{x}_e > \overline{x}_i, \end{cases}$$

$$\frac{\partial d_{e,i-1}}{\partial \overline{y}_i} = \begin{cases} 0, & \text{if } \overline{x}_e < \overline{x}_{i-1}, \\ \text{sign}\left(|\mathbf{G}_{e,i}|\right)\left(\dfrac{\overline{x}_e - \overline{x}_{i-1}}{l_i} - \dfrac{\det|\mathbf{G}_{e,i}|}{l_i^2}\dfrac{\partial l_{i-1}}{\partial \overline{y}_i}\right), & \text{if } \overline{x}_i \leqslant \overline{x}_e \leqslant \overline{x}_{i+1}, \\ \dfrac{(\overline{y}_i - \overline{y}_e)}{\sqrt{(\overline{x}_e - \overline{x}_i)^2 + (\overline{y}_e - \overline{y}_i)^2}}, & \text{if } \overline{x}_e > \overline{x}_i, \end{cases} \quad (29)$$

$$\frac{\partial d_{e,i}}{\partial \overline{x}_e} =
\begin{cases}
\dfrac{(\overline{x}_e - \overline{x}_i)}{\sqrt{(\overline{x}_e - \overline{x}_i)^2 + (\overline{y}_e - \overline{y}_i)^2}}, & \text{if } \overline{x}_e < \overline{x}_i, \\[3mm]
\text{sign}\left(\left|\mathbf{G}_{e,i}\right|\right)\left(\dfrac{\overline{y}_{i+1} - \overline{y}_i}{l_i} - \dfrac{\det\left|\mathbf{G}_{e,i}\right|}{l_i^2}\dfrac{\partial l_i}{\partial \overline{x}_e}\right), & \text{if } \overline{x}_i \le \overline{x}_e \le \overline{x}_{i+1}, \\[3mm]
\dfrac{(\overline{x}_e - \overline{x}_{i+1})}{\sqrt{(\overline{x}_e - \overline{x}_{i+1})^2 + (\overline{y}_e - \overline{y}_{i+1})^2}}, & \text{if } \overline{x}_e > \overline{x}_{i+1},
\end{cases}$$

$$\frac{\partial d_{e,i}}{\partial \overline{y}_e} =
\begin{cases}
\dfrac{(\overline{y}_e - \overline{y}_i)}{\sqrt{(\overline{x}_e - \overline{x}_i)^2 + (\overline{y}_e - \overline{y}_i)^2}}, & \text{if } \overline{x}_e < \overline{x}_i, \\[3mm]
\text{sign}\left(\left|\mathbf{G}_{e,i}\right|\right)\left(\dfrac{\overline{x}_i - \overline{x}_{i+1}}{l_i} - \dfrac{\det\left|\mathbf{G}_{e,i}\right|}{l_i^2}\dfrac{\partial l_i}{\partial \overline{y}_e}\right), & \text{if } \overline{x}_i \le \overline{x}_e \le \overline{x}_{i+1}, \\[3mm]
\dfrac{(\overline{y}_e - \overline{y}_{i+1})}{\sqrt{(\overline{x}_e - \overline{x}_{i+1})^2 + (\overline{y}_e - \overline{y}_{i+1})^2}}, & \text{if } \overline{x}_e > \overline{x}_{i+1}.
\end{cases} \tag{30}$$

The derivatives $\partial \overline{x}_i / \partial x_i$, $\partial \overline{x}_i / \partial y_i$ can be calculated as

$$\frac{\partial \overline{x}_i}{\partial x_i} = \frac{\partial \frac{x_{i+1} - x_i}{l_i}}{\partial x_i} x_i + \frac{x_{i+1} - x_i}{l_i} + \frac{\partial \frac{y_{i+1} - y_i}{l_i}}{\partial x_i} y_i,$$

$$\frac{\partial \overline{x}_i}{\partial y_i} = \frac{\partial \frac{x_{i+1} - x_i}{l_i}}{\partial y_i} x_i + \frac{\partial \frac{y_{i+1} - y_i}{l_i}}{\partial y_i} y_i + \frac{y_{i+1} - y_i}{l_i}. \tag{31}$$

The derivatives $\partial \overline{y}_i / \partial \xi_i$, $\partial \overline{x}_{i+1} / \partial \xi_i$, $\partial \overline{y}_{i+1} / \partial \xi_i$, $\partial \overline{x}_e / \partial \xi_i$ and $\partial \overline{y}_e / \partial \xi_i$ can be calculated in the same way.

$$\frac{\partial f_k}{\partial \xi_i} =
\begin{cases}
\dfrac{1}{l_k l_{k+1}}\dfrac{\partial B_k}{\partial \xi_i} - \dfrac{B_k}{l_k^2 l_{k+1}}\dfrac{\partial l_k}{\partial \xi_i} - \dfrac{B_k}{l_k l_{k+1}^2}\dfrac{\partial l_{k+1}}{\partial \xi_i}, & k = i-2, i-1, i, \quad i = 1,2,\dots,N_{\text{node}}, \\[3mm]
0, & k = -1, 0, N_{\text{node}} - 1, N_{\text{node}}.
\end{cases} \tag{33}$$

The derivatives $\partial B_i / \partial x_i$, $\partial B_{i-1} / \partial x_i$, and $\partial B_{i-2} / \partial x_i$ can be calculated as

$$\frac{\partial B_i}{\partial x_i} = x_{i+2} - x_{i+1},$$

$$\frac{\partial B_{i-1}}{\partial x_i} = -(x_{i+1} - x_i) - (x_{i-1} - x_i), \tag{34}$$

$$\frac{\partial B_{i-2}}{\partial x_i} = x_{i-2} - x_{i-1}.$$

The derivatives $\partial l_{i+1} / \partial x_i$, $\partial l_i / \partial x_i$, $\partial l_{i-1} / \partial x_i$, and $\partial l_{i-2} / \partial x_i$ can be calculated as

$$\frac{\partial l_{i+1}}{\partial x_i} = 0,$$

$$\frac{\partial l_i}{\partial x_i} = -\frac{x_{i+1} - x_i}{l_i},$$

$$\frac{\partial l_{i-1}}{\partial x_i} = \frac{x_i - x_{i-1}}{l_{i-1}}, \tag{35}$$

$$\frac{\partial l_{i-2}}{\partial x_i} = 0.$$

Finally, the derivatives $\partial B_i / \partial y_i$, $\partial B_{i-1} / \partial y_i$, $\partial B_{i-2} / \partial y_i$, $\partial l_{i+1} / \partial y_i$, $\partial l_i / \partial y_i$, $\partial l_{i-1} / \partial y_i$, and $\partial l_{i-2} / \partial y_i$ can be calculated in the same way.

3.2.2 Sensitivities analysis of constraints on the angle between adjacent bars

The derivatives of the aggregated angle constraint function A (see Eq. (13)) with respect to design variables $\xi_i = x_i$, y_i $\left(i = 1, 2, ..., x_{N_{\text{node}}}\right)$ can be calculated by

$$\frac{\partial A}{\partial \xi_i} = \frac{\sum_{k=i-2}^{i} e^{p_{\text{KS}}(f_k - f_{\max})} \frac{\partial f_k}{\partial \xi_i}}{\sum_{k=1}^{N_{\text{node}}} e^{p_{\text{KS}}(f_k - f_{\max})}}, \tag{32}$$

$$i = 1,2,\dots,N_{\text{node}}, \quad k > 0,$$

where

3.2.3 Sensitivities analysis of internal points boundary constraints

The derivation of the aggregated constraints function of internal point Δ (see Eq. (18)) with respect to design variables $\xi_i = x_i$, y_i, $\left(i = 1, 2,, \cdots, x_{N_{\text{node}}}\right)$ can be calculated by

$$\frac{\partial \Delta}{\partial \xi_i} = \frac{\sum_{j=i-1}^{i} \sum_{q=0}^{m} e^{p_{\text{KS}}[\delta(\xi_{j,q}) - \delta_{\max}(\xi)]} \frac{\partial \delta(\xi_{j,q})}{\partial \xi_i}}{\sum_{i=1}^{N_{\text{node}} - 1} \sum_{q=0}^{m} e^{p_{\text{KS}}[\delta(\xi_{i,q}) - \delta_{\max}(\xi)]}}, \tag{36}$$

$$i = 1,2,\cdots,N_{\text{node}}, \quad j > 0.$$

4. Numerical examples

In this section, three numerical examples of chain-like structures are tested to illustrate the effectiveness of the proposed feature-driven topology optimization method preserving the component sequences. The bar with semi-circular ends is used as a basic parameterization geometry feature. The method of moving asymptotes (MMA) [64] is employed as the optimizer. For all problems in this section, Young's modulus is $E = 1$, Poisson's ratio is $v = 0.3$, and a

concentrated unit force is $F = 1$. The geometry is defined in dimensionless coordinates. The width of each bar with semi-circular ends is 2.

4.1 Numerical example 1: A short beam with a vertical load at the right bottom corner

As shown in Fig. 6, the rectangular design domain is discretized with 160×80 plane stress elements. The lower and upper bounds on design variables (x_i, y_i) $(i = 1, 2, \cdots, N_{node})$ are set as $\{0, 0\}$ and $\{120, 60\}$, respectively. This benchmark example of a cantilever beam subjected to a vertical force at the right bottom corner [54] is solved to verify the effectiveness of the chain-of-bars design variables setting scheme. The moving bars are connected end-to-end to represent the manufacturing path of the structure. The coordinates of the nodes in a chain of bars are used as design variables. The compliance is minimized, and the constraint on the volume fraction of $VF \leq 0.36$ is imposed.

Three different initial layouts of the chain of bars (see Fig. 7) are used to study their influence on the optimization results. The numbers of bars, nodes, and design variables in these three cases are listed in Table 2. The arrow lines on the bar segments represent the path of moving the 3D printing head. The number of bars increases from Fig. 7a to b to c.

Taking Case 1 as an example, $34 \times 4 = 136$ design variables and 33 additional constraints should be used in the free-form feature-driven topology optimization method. However, for the feature-driven method with the chain-of-bars design variables setting scheme, only $(34 + 1) \times 2 = 70$
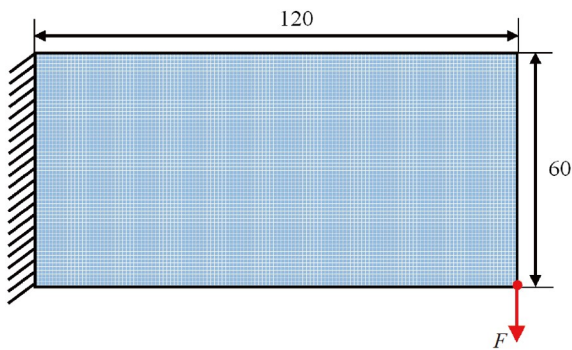

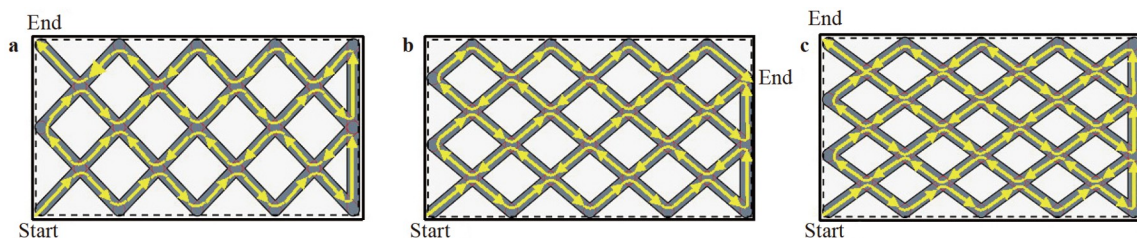**Figure 6** A short beam with a vertical load at the bottom right corner $L \times H = 120 \times 60$.

Table 2 Three design variables setting cases for the short beam

Case	Number of bars	Number of nodes	Number of design variables
1	34	35	70
2	42	43	86
3	51	52	104

design variables and no additional constraints are used.

Figure 8 shows the results in Cases 1-3 using the free-form feature-driven topology optimization method. The arrow lines represent the path of moving the 3D printing head. It is observed that a more significant number of design variables contributes to the appearance of detailed structures. Apart from some moving bar features working on the main structure topology, several 0-length bars are shown as overhanging circular islands inside the design domain. The overhanging circular islands are counted in structural volume and the length of the printing path; however, they bear no load. Therefore, they should be cleaned up by post-processing. Additionally, some lines are out of bars, which means the 3D printing head needs to suspend ejecting material and cut the continuous carbon fibre when passing those routes. Finally, compliance and volume fraction convergence histories of Cases 2 and 3 are plotted, as shown in Fig. 9.

In addition, the same initial cases (see Fig. 7) are used to compare the free-form feature-driven method with the feature-driven method using the chain-of-bars design variables setting scheme under the same volume fraction constraint. Figure 10 shows the results of the feature-driven topology optimization method with the chain-of-bars design variables setting scheme. The arrow lines on the bar segments represent the path of the moving 3D printing head. With the different initial configurations, it can be observed that the optimized results are different topologies with similar values of compliance. Because this method establishes the chain-like printing path in a straightforward way, the total length of bars is efficiently controlled to be of the desired value (Table 3). The values of structural compliance corresponding to 49.30, 48.72, and 47.34 show a decreased tendency with the increase of the total number of design variables. The optimized compliance using the chain-of-bars design variables setting scheme increases by 9.78%, 11.47%, and 7.86%, respectively, as compared to free-form optimization
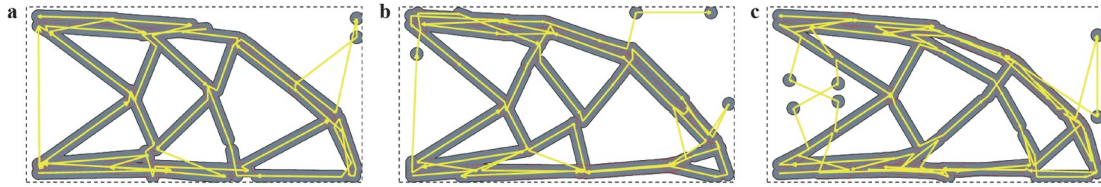

Figure 7 Initial layouts of the chain of bars within a design domain. **a** Case 1. **b** Case 2. **c** Case 3.

Figure 8 Results of original free-form feature-driven topology optimization with useless overhanging islands and longer length of the path in three cases. **a** Case 1. **b** Case 2. **c** Case 3.
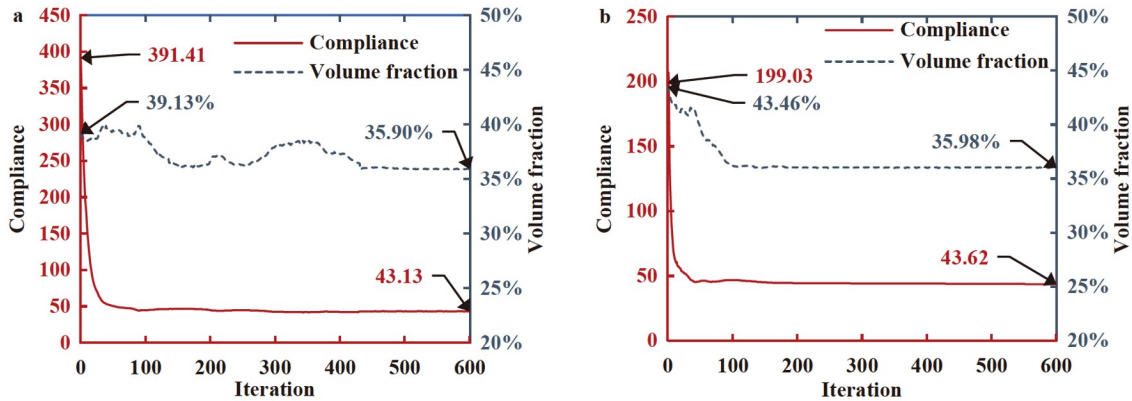

Figure 9 Convergence curves of compliance and volume fraction for free-form topology optimization. **a** Case 2. **b** Case 3.
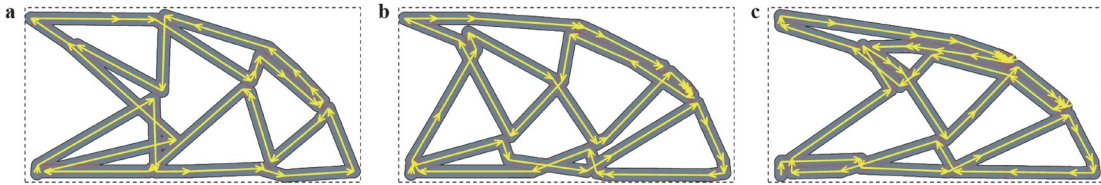

Figure 10 Results of the feature-driven topology optimization with the chain-of-bars design variables setting scheme. **a** Case 1. **b** Case 2. **c** Case 3.

Table 3 Comparison of the total length of the 3D printing path for the free-form feature-driven method and feature-driven method with the chain-of-bars design variable setting scheme in three cases

Case	Free-form feature-driven method	Feature-driven method with the chain-of-bars design variable setting scheme	Total length decrease
1	779.57	699.81	11.40%
2	763.26	699.85	9.06%
3	811.15	699.17	16.02%

results because the chain design variables setting scheme involves additional limitations for topology optimization. The optimization results with the chain-of-bars design variables setting scheme are similar to those of the free-form feature-driven method (see Figs. 8 and 10). The convergence histories of structural compliance and constraints of the feature-driven method with chain-of-bars design variables setting scheme in Cases 2 and 3 are shown in Fig. 11. Due to the relatively large optimization length step and the violation of constraints, the compliance shows significant oscillations at the start of the optimization process. All cases converged and satisfied the prescribed constraints.

Additionally, the comparison of computation costs be-

tween the two methods (the proposed method using the chain-of-bars design variables setting scheme and the original feature-driven method with additional chain constraints) to solve the same chain-like structural optimization problem (Fig. 6) with the initial layout of the chain of bars (Case 1 in Fig. 7a) is shown in Table 4. The computer hardware used to solve all the problems is a 3.19 GHz 16-Core 12th Gen Intel Core i9, running Windows 10 Professional 19044.2364 and the software is MATLAB R2019b. Note the remarkably short computational time of the proposed method using the chain-of-bars design variables setting scheme. Converging in the same number of iterations (400), the optimization time using the original feature-dri-
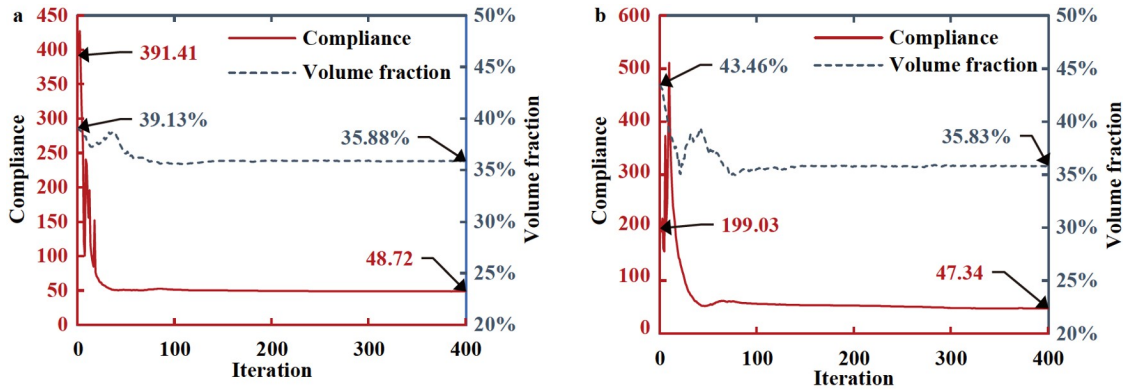
Figure 11　Convergence curves of compliance and volume fraction of the feature-driven method with chain-of-bars design variables setting scheme. **a** Case 2. **b** Case 3.

Table 4　Comparison of computation costs

	Original feature-driven method with additional chain constraints	Chain-of-bars method
Number of iterations	400	400
Overall elapsed time (s)	5894	3485

Table 5　The angle constraints for the short beam

Angle constraints	Range of angle β
Condition 1	without constraint
Condition 2	[30°, 330°]
Condition 3	[37.5°, 322.5°]

ven method with additional chain constraints takes 5894 s. In comparison, the method based on the chain-of-bars design variables setting scheme takes 3485 s. It demonstrates that the proposed method is more efficient than the original feature-driven method.

4.2　Numerical example 2: A short beam with a vertical load at the middle point of the right side

Unlike the previous numerical example, the design domain is the size of 120×75 and a concentrated vertical force is applied at the middle point of the right side, as depicted in Fig. 12. The design domain is discretized into 160×80 plane stress elements. The initial configuration of Case 3 in Fig. 7 is chosen in this section. This example is intended to illustrate the effectiveness of angle constraints β on the optimization results. Different lower bound values $\beta = 0°$, 30°, and 37.5° on the angles are considered in Table 5.

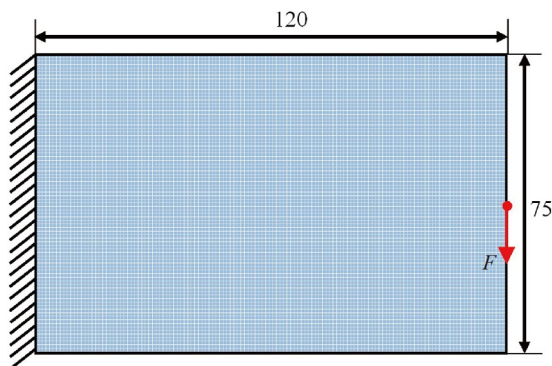**Figure 12**　A short beam with a vertical load at the mid-point of the right side $L \times H = 120 \times 75$.

In this method, the angles between adjacent bars are efficiently controlled using an analytical function A (see Eq. (13)). Optimized topologies corresponding to minimum angle constraints $\beta \geq 0°$, 30°, and 37.5° are obtained after the movement of endpoint coordinates of bars and are shown in Fig. 13 (left). The path of the moving 3D printing head is shown in arrow lines on the bar segments. It is observed that a more considerable value of angle constraint leads to additional difficulties in achieving higher stiffness structures, which is indicated by the increase in compliance. The compliance optimized with angle constraints (30° and 37.5°) increases by 7.26% and 8.42%, respectively, as compared to optimized results without angle constraints listed in Table 6. The angle constraint helps to avoid manufacturing defects caused by sharp angle problems. In Fig. 13b and c, every angle of 3D printing is constrained to be larger than 30° and 37.5°, respectively, which corresponds to different printing quality on printing angles. On the contrary, the angles of 3D printing are not constrained in Fig. 13a, and a small 27.1° angle occurs and is marked by a circle. The convergence histories of compliance and total length constraint are shown in Fig. 13 (right). Due to the relatively large optimization length step and the violation of other constraints, the compliance shows significant oscillations at the start of the optimization process. All cases converged and satisfied the prescribed total length and angle constraints within acceptable violation (0.005).

4.3　Numerical example 3: Frame of a satellite antenna

In this numerical example, the frame structure of a satellite antenna is used to verify the effectiveness of the total length
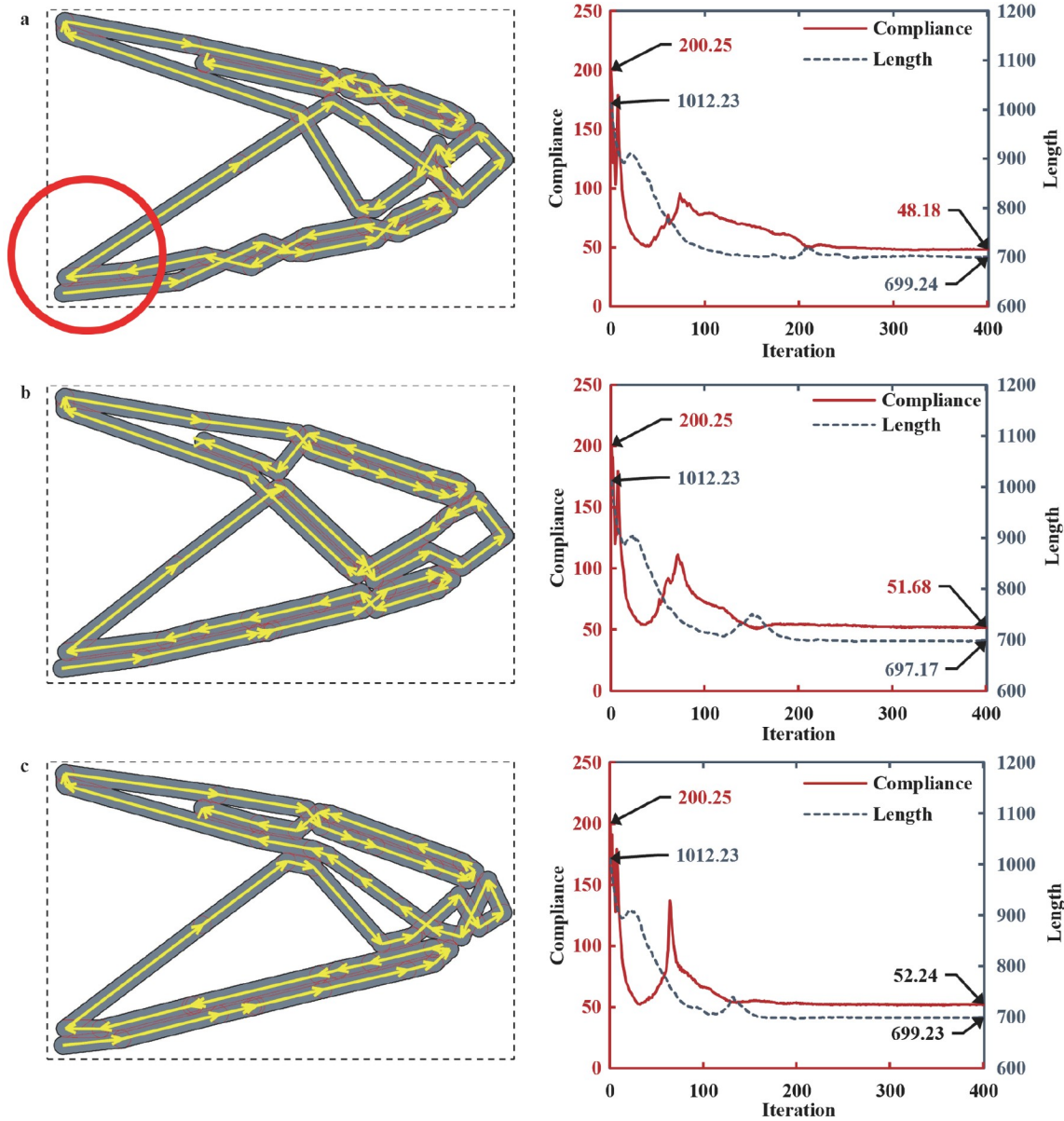
Figure 13 Optimized results (left) and convergence histories of compliance and total length (right) of the feature-driven method preserving component sequence with a series of angle constraints. **a** $\beta \geq 0°$. **b** $\beta \geq 30°$. **c** $\beta \geq 37.5°$.

Table 6 Optimized compliance comparison for different angles

$\beta > 0°$	$\beta > 30°$		$\beta > 37.5°$	
Compliance	Compliance	Increase	Compliance	Increase
48.18	51.68	7.26%	52.24	8.42%

constraint. Due to symmetry, half of the model (of the size of 100×70) is considered, as shown in Fig. 14 [65]. The left-hand side of the design domain is fixed, and a unit-concentrated vertical point load is imposed on the top right corner.

The initial configuration with 51 connected moving bars is used, as shown in Fig. 15a. The optimization result without total length constraint is shown in Fig. 15b, with many in-efficient printed parts overhanging in the design domain.
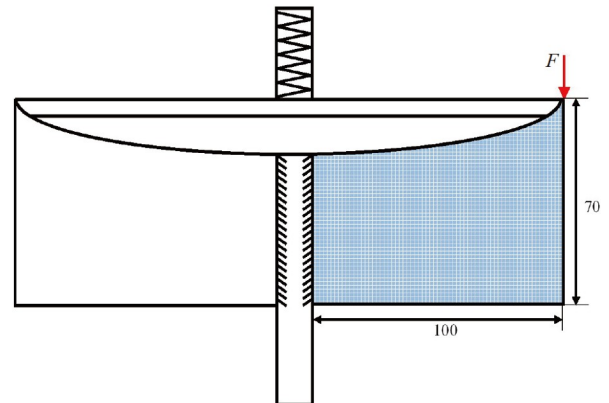

Figure 14 Optimization setting and boundary condition of satellite antenna [65].
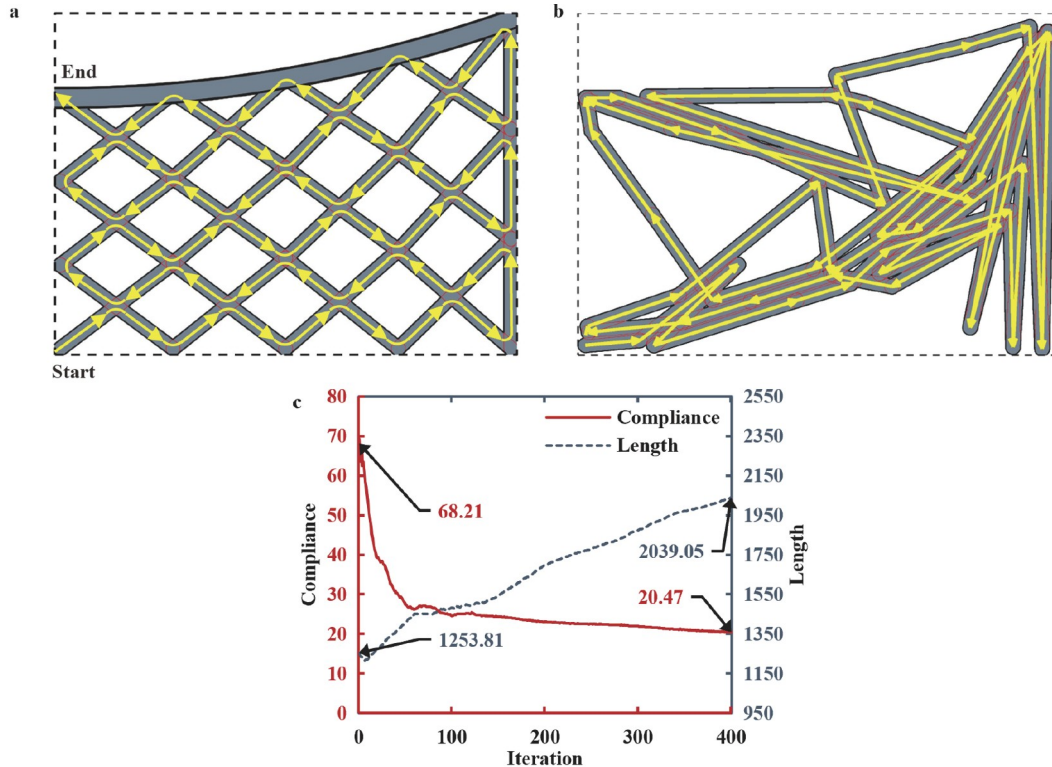
Figure 15 Feature-driven topology optimization method without total length constraint. **a** The initial layout of 51 connected moving bars. **b** The optimized result. **c** The convergence curves of compliance and total length.

Finally, the compliance and total length convergence curves are plotted in Fig. 15c.

Next, the effect of the upper bound on L is studied using the values of 1000, 1100, 1200, and 1300. The optimization results are shown in Fig. 16. In this method, the total length of the 3D printing path is efficiently controlled by using a compact analytical function of the total length function L (see Eq. (10)) because the design variables are nodal co-ordinates of the ends of moving bars.

The compliance values and their increases due to different total length constraints of optimization results in four cases are listed in Table 7. It shows that the tendency of compliance decreases with the increase of the total length constraint value. The convergence curves of compliance and total length constraints are plotted in Fig. 17. In the beginning, the compliance changes sharply because the total length constraints have not been met yet. Finally, all cases converge and satisfy the prescribed total length constraints.

5. Conclusions

This study presents a feature-driven topology optimization method preserving component sequences. The sequence requirement is satisfied by the chain-of-bars design variables setting scheme, and the interdependent relationship among structural components can be controlled by constraints related to manufacturing requirements.

Numerical examples show that the method can directly control the component sequences and be used for minimum compliance design problems under total length, volume fraction, and angle between adjacent bars constraints. Compared to other methods reviewed in this study, this method has the following positive features: (1) the inter-dependence of sub-structures is analytically controlled by the design variables setting scheme; (2) it needs only approximately half the number of design variables and no additional constraints to obtain a chain-like structure design as compared to the original feature-driven method, and opens up new possibilities for structure design and manufacturing; (3) it can address the challenge of handling a sharp turning angle in the manufacturing process by introducing angle constraint.

In the future, the proposed method is planned to be extended to orthotropic material properties and the 3D material model considering joint effect for the application of AM-CFRP structures. Each element will be assigned with anisotropic material properties. In the crossover region of the print path, the carbon fibre filament will be repeatedly placed. Thus, the material properties of elements inside the crossover region should be enhanced in each direction of the placed filament. Consequently, the stiffness of elements in the crossover region is significantly enhanced compared
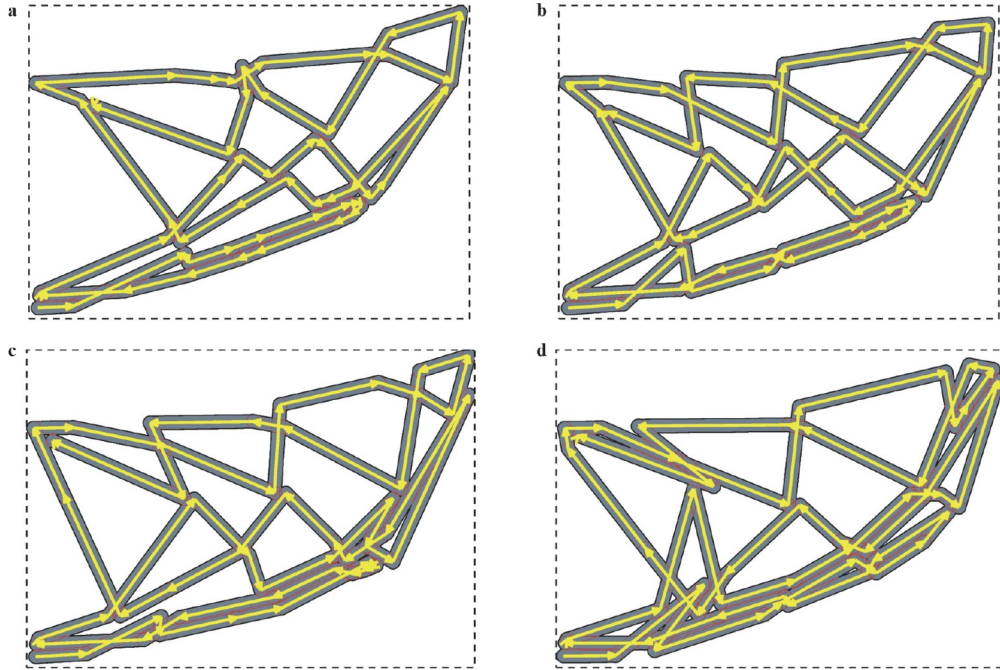
Figure 16 Optimized results with different values of the total length constraints *L*. **a** *L* ≤ 1000. **b** *L* ≤ 1100. **c** *L* ≤ 1200. **d** *L* ≤ 1300.

Table 7 Comparison of minimized compliance for different total length *L*

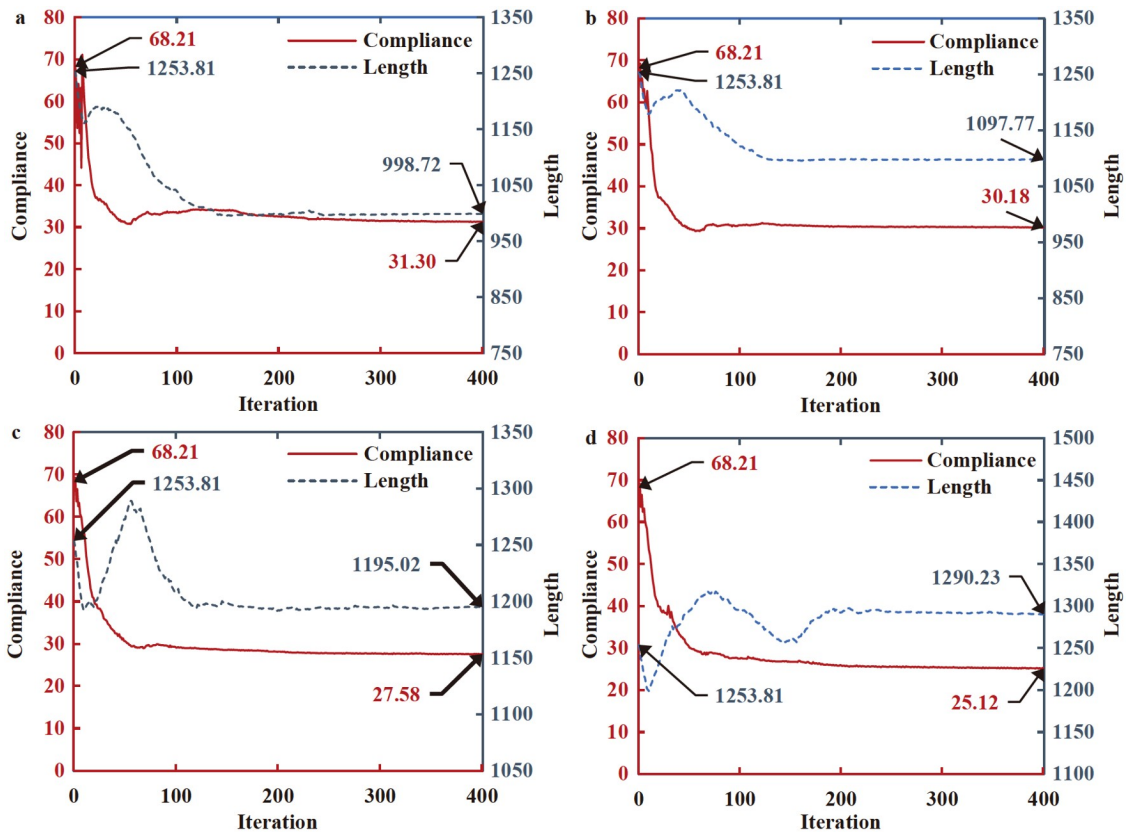| Items	$L \leq 1000$	$L \leq 1100$	$L \leq 1200$	$L \leq 1300$	$L \leq +\infty$
Compliance	31.30	30.18	27.58	25.12	20.47
Compliance increases	52.91%	47.44%	34.73%	22.72%	0.00%

Figure 17 Convergence histories with different total length constraints *L*. **a** *L* ≤ 1000. **b** *L* ≤ 1100. **c** *L* ≤ 1200. **d** *L* ≤ 1300.

D. Jia, *et al. Acta Mech. Sin.*, Vol. 40, 423433 (2024)

423433-15

with that in other regions, which is aligned with the actual filament distribution and benefits the strength and stiffness at the joint.

For larger-scale structural design problems, the printing head should go back and forth several times when filling a bar with material ejected from the 3D printing head. Thus, the number of nodes to describe the 3D printing trajectories will significantly increase. Therefore, a path planning method to form a parallel trajectory will be developed to reduce the number of nodes to describe the 3D printing trajectory. Also, the proposed method has advantages in designing thin-wall lattice structures. Future work should investigate the performance of lattice structures designed by the feature-driven method preserving component sequences. Other extensions are the consideration of 3-dimensional and multi-disciplinary problems.

1   Y. Liu, B. Shaw, M. D. Dickey, and J. Genzer, Sequential self-folding of polymer sheets, Sci. Adv. **3**, e1602417 (2017).

2   M. Bi, L. Xia, P. Tran, Z. Li, Q. Wan, L. Wang, W. Shen, G. Ma, and Y. M. Xie, Continuous contour-zigzag hybrid toolpath for large format additive manufacturing, Addit. Manuf. **55**, 102822 (2022).

3   I. Fidan, A. Imeri, A. Gupta, S. Hasanov, A. Nasirov, A. Elliott, F. Alifui-Segbaya, and N. Nanami, The trends and challenges of fiber reinforced additive manufacturing, Int. J. Adv. Manuf. Technol. **102**, 1801 (2019).

4   F. Baumann, J. Scholz, and J. Fleischer, Investigation of a new approach for additively manufactured continuous fiber-reinforced polymers, Procedia CIRP **66**, 323 (2017).

5   J. Zhu, H. Zhou, C. Wang, L. Zhou, S. Yuan, and W. Zhang, A review of topology optimization for additive manufacturing: Status and challenges, Chin. J. Aeronaut. **34**, 91 (2021).

6   K. Yamamoto, J. V. S. Luces, K. Shirasu, Y. Hoshikawa, T. Okabe, and Y. Hirata, A novel single-stroke path planning algorithm for 3D printers using continuous carbon fiber reinforced thermoplastics, Addit. Manuf. **55**, 102816 (2022).

7   P. Appendino, F. Della Ferrera, D. Nassisi, G. Blandino, E. Gino, S. D. Solla, and M. G. Ruo Redda, Are intraoral customized stents still necessary in the era of Highly Conformal Radiotherapy for Head & Neck cancer? Case series and literature review, Rep. Pract. Oncol. RadioTher. **24**, 491 (2019).

8   W. Hu, G. Z. Lum, M. Mastrangeli, and M. Sitti, Small-scale soft-bodied robot with multimodal locomotion, Nature **554**, 81 (2018).

9   Q. Wang, J. A. Jackson, Q. Ge, J. B. Hopkins, C. M. Spadaccini, and N. X. Fang, Lightweight mechanical metamaterials with tunable negative thermal expansion, Phys. Rev. Lett. **117**, 175901 (2016).

10   M. Schenk, and S. D. Guest, Geometry of Miura-folded metamater-

11   J. Ma, H. Feng, Y. Chen, D. Hou, and Z. You, Folding of tubular waterbomb, Research **2020**, 1735081 (2020).

12   B. An, S. Miyashita, M. T. Tolley, D. M. Aukes, L. Meeker, E. D. Demaine, M. L. Demaine, R. J. Wood, and D. Rus, in An end-to-end approach to making self-folded 3D surface shapes by uniform heating: Proceedings of the 2014 IEEE International Conference on Robotics and Automation (ICRA), Hong Kong, 2014, pp. 1466-1473.

13   D. Jia, P. Feng, L. Wang, L. Chen, J. Wang, J. Zhu, Y. Xu, and W. Zhang, An origami shield with supporting frame structures optimized by a feature-driven topology optimization method, Def. Technol. **31**, 447 (2024).

14   M. Wüthrich, W. J. Elspass, P. Bos, and S. Holdener, Novel 4-Axis 3D Printing Process to Print Overhangs without Support Material (Springer, Cham, 2021), pp. 130-145.

15   G. Alonayni, and M. I. Campbell, in Build orientation optimization for five-axis 3D printing: Proceedings of the ASME 2023 International Design Engineering Technical Conferences and Computers and Information in Engineering Conference, Boston, 2023, pp. 20-23.

16   H. Liu, L. Liu, D. Li, R. Huang, and N. Dai, An approach to partition workpiece CAD model towards 5-axis support-free 3D printing, Int. J. Adv. Manuf. Technol. **106**, 683 (2020).

17   M. Wang, H. Zhang, Q. Hu, D. Liu, and H. Lammer, Research and implementation of a non-supporting 3D printing method based on 5-axis dynamic slice algorithm, Robot. Comput.-Integr. Manuf. **57**, 496 (2019).

18   I. M. Lei, Y. Sheng, C. L. Lei, C. Leow, and Y. Y. S. Huang, A hackable, multi-functional, and modular extrusion 3D printer for soft materials, Sci. Rep. **12**, 12294 (2022).

19   M. T. Mollah, A. Moetazedian, A. Gleadall, J. Yan, W. E. Alphonso, R. B. Comminal, B. Seta, T. Lock, and J. Spangenberg, in Investigation on corner precision at different corner angles in material extrusion additive manufacturing: An experimental and computational fluid dynamics analysis: Proceedings of the 2022 International Solid Freeform Fabrication Symposium, Austin, 2022.

20   M. A. Quetzeri-Santiago, C. L. Hedegaard, and J. R. Castrejón-Pita, Additive manufacturing with liquid latex and recycled end-of-life rubber, 3D Print. Addit. Manuf. **6**, 149 (2019).

21   H. Gau, S. Herminghaus, P. Lenz, and R. Lipowsky, Liquid morphologies on structured surfaces: From microchannels to microchips, Science **283**, 46 (1999).

22   R. Comminal, M. P. Serdeczny, D. B. Pedersen, and J. Spangenberg, Motion planning and numerical simulation of material deposition at corners in extrusion additive manufacturing, Addit. Manuf. **29**, 100753 (2019).

23   F. Ferrari, B. S. Lazarov, and O. Sigmund, Eigenvalue topology optimization via efficient multilevel solution of the frequency response, Int. J. Numer. Methods Eng. **115**, 872 (2018).

24   H. Ghasemi, H. S. Park, and T. Rabczuk, A level-set based IGA formulation for topology optimization of flexoelectric materials, Comput. Methods Appl. Mech. Eng. **313**, 239 (2017).

25   M. P. Bendsøe, and N. Kikuchi, Generating optimal topologies in structural design using a homogenization method, Comput. Methods Appl. Mech. Eng. **71**, 197 (1988).

26   M. Zhou, and G. I. N. Rozvany, The COC algorithm, Part II: Topological, geometrical and generalized shape optimization, Comput. Methods Appl. Mech. Eng. **89**, 309 (1991).

27   E. Andreassen, F. Ferrari, O. Sigmund, and A. R. Diaz, Frequency response as a surrogate eigenvalue problem in topology optimization, Int. J. Numer. Methods Eng. **113**, 1214 (2018).

28   Q. Chen, X. Zhang, and B. Zhu, Design of buckling-induced mechanical metamaterials for energy absorption using topology optimization, Struct. Multidisc. Optim. **58**, 1395 (2018).

29   J. T. Liu, and H. C. Gea, Robust topology optimization under multiple independent unknown-but-bounded loads, Comput. Methods Appl. Mech. Eng. **329**, 464 (2018).

30   T. Gao, and W. Zhang, Topology optimization involving thermo-

ials, Proc. Natl. Acad. Sci. U.S.A. **110**, 3276 (2013).

D. Jia, *et al. Acta Mech. Sin.*, Vol. 40, 423433 (2024)

423433-16

elastic stress loads, Struct. Multidisc. Optim. **42**, 725 (2010).

31 M. P. Bendsøe, Optimal shape design as a material distribution problem, Struct. Optim. **1**, 193 (1989).

32 X. Chen, C. Li, and Y. Bai, Topology optimization of sandwich structures with solid-porous hybrid infill under geometric constraints, Comput. Methods Appl. Mech. Eng. **382**, 113856 (2021).

33 N. Wei, H. Ye, X. Zhang, W. Wang, and Y. Sui, Lightweight topology optimization of graded lattice structures with displacement constraints based on an independent continuous mapping method, Acta Mech. Sin. **38**, 421352 (2022).

34 Q. Li, Y. Qu, Y. Luo, and S. Liu, Concurrent topology optimization design of stiffener layout and cross-section for thin-walled structures, Acta Mech. Sin. **37**, 472 (2021).

35 Z. Chen, G. Wen, H. Wang, L. Xue, and J. Liu, Multi-resolution nonlinear topology optimization with enhanced computational efficiency and convergence, Acta Mech. Sin. **38**, 421299 (2022).

36 W. Dong, Y. Li, K. Xin, D. Yin, L. Song, and T. Gao, A method of designing plate structure consisting of lattices and stiffeners based on topology optimization, J. Northwest. Polytech. Univ. **39**, 1233 (2021).

37 W. Zhang, G. Dai, F. Wang, S. Sun, and H. Bassir, Using strain energy-based prediction of effective elastic properties in topology optimization of material microstructures, Acta Mech. Sin. **23**, 77 (2007).

38 Y. M. Xie, and G. P. Steven, A simple evolutionary procedure for structural optimization, Comput. Struct. **49**, 885 (1993).

39 Y. M. Xie, and G. P. Steven, Basic Evolutionary Structural Optimization (Springer, London, 1997).

40 X. Huang, and Y. M. Xie, Evolutionary Topology Optimization of Continuum Structures: Methods and Applications (Wiley, Chichester, 2010).

41 J. A. Sethian, and A. Wiegmann, Structural boundary design via level set and immersed interface methods, J. Comput. Phys. **163**, 489 (2000).

42 K. Yaji, T. Yamada, M. Yoshino, T. Matsumoto, K. Izui, and S. Nishiwaki, Topology optimization in thermal-fluid flow using the lattice Boltzmann method, J. Comput. Phys. **307**, 355 (2016).

43 B. Zhu, R. Wang, H. Li, and X. Zhang, A level set method with a bounded diffusion for structural topology optimization, J. Mech. Des. **140**, 071402 (2018).

44 L. Chen, J. Wan, X. Chu, and H. Liu, Parameterized level set method for structural topology optimization based on the Cosserat elasticity, Acta Mech. Sin. **37**, 620 (2021).

45 K. Liang, J. He, Z. Jia, and X. Zhang, Topology optimization of magnetorheological smart materials included PnCs for tunable wide bandgap design, Acta Mech. Sin. **38**, 421525 (2022).

46 Z. Du, X. Y. Zhou, R. Picelli, and H. A. Kim, Connecting microstructures for multiscale topology optimization with connectivity index constraints, J. Mech. Des. **140**, 111417 (2018).

47 O. M. Querin, M. Victoria, C. Alonso, R. Ansola, and P. Martí, Chapter 1—Introduction, in: O. M. Querin, M. Victoria, C. Alonso, R. Ansola, and P. Martí, eds. Topology Design Methods for Structural Optimization, (Academic Press, Oxford, 2017), pp. 1-13.

48 M. Zhou, R. Fleury, and M. Kemp, in Optimization of composite—Recent advances and application: Proceedings of the 13th AIAA/ ISSMO Multidisciplinary Analysis Optimization Conference, American Institute of Aeronautics and Astronautics, Fort Worth, 2010, p. 9272.

49 H. H. Gao, J. H. Zhu, W. H. Zhang, and Y. Zhou, An improved adaptive constraint aggregation for integrated layout and topology optimization, Comput. Methods Appl. Mech. Eng. **289**, 387 (2015).

50 L. P. Jiu, Y. Zhou, J. H. Zhu, and W. H. Zhang, Feature-driven method for structural topology optimization (in Chinese), Sci. Sin. Tech. **49**, 1177 (2019).

51 Z. Xu, W. Zhang, Y. Zhou, and J. Zhu, Multiscale topology optimization using feature-driven method, Chin. J. Aeronaut. **33**, 621 (2020).

52 Y. Zhou, H. Zhan, W. Zhang, J. Zhu, J. Bai, Q. Wang, and Y. Gu, A new data-driven topology optimization framework for structural optimization, Comput. Struct. **239**, 106310 (2020).

53 Y. Zhou, W. Zhang, and J. Zhu, Concurrent shape and topology optimization involving design-dependent pressure loads using implicit B-spline curves, Int. J. Numer. Methods Eng. **118**, 495 (2019).

54 Y. Zhou, W. Zhang, J. Zhu, and Z. Xu, Feature-driven topology optimization method with signed distance function, Comput. Methods Appl. Mech. Eng. **310**, 1 (2016).

55 S. Cai, and W. Zhang, Stress constrained topology optimization with free-form design domains, Comput. Methods Appl. Mech. Eng. **289**, 267 (2015).

56 F. Wein, P. D. Dunning, and J. A. Norato, A review on feature-mapping methods for structural optimization, Struct. Multidisc. Optim. **62**, 1597 (2020).

57 J. H. Zhu, P. Beckers, and W. H. Zhang, On the multi-component layout design with inertial force, J. Comput. Appl. Math. **234**, 2222 (2010).

58 V. N. Hoang, and G. W. Jang, Topology optimization using moving morphable bars for versatile thickness control, Comput. Methods Appl. Mech. Eng. **317**, 153 (2017).

59 L. Zhou, and W. Zhang, Topology optimization method with elimination of enclosed voids, Struct. Multidisc. Optim. **60**, 117 (2019).

60 W. Zhang, and L. Zhou, Topology optimization of self-supporting structures with polygon features for additive manufacturing, Comput. Methods Appl. Mech. Eng. **334**, 56 (2018).

61 S. Y. Woon, O. M. Querin, and G. P. Steven, On improving the GA step-wise shape optimization method through the application of the Fixed Grid FEA paradigm, Struct. Multidisc. Optim. **25**, 270 (2003).

62 G. Kreisselmeier, and R. Steinhauser, Systematic control design by optimizing a vector performance index, IFAC Proc. Volumes **12**, 113 (1979).

63 G. Taubin, Distance approximations for rasterizing implicit curves, ACM Trans. Graph. **13**, 3 (1994).

64 K. Svanberg, The method of moving asymptotes—A new method for structural optimization, Int. J. Numer. Methods Eng. **24**, 359 (1987).

65 J. Rong, J. Li, and T. Xu, Numerical investigation of dynamic response of CE-1 directional antenna. Spacecr. Eng. **20**, 81 (2011).

考虑转角约束的特征驱动拓扑优化方法

贾东升, 刘磊, 朱继宏, 张煜, Vassili Toropov

摘要 保持组件顺序是一些典型结构(如可展开的链状结构、平行打印路径的3D打印结构、连续纤维增强聚合物增材制造结构、定制支架和软机器人部件)的实际工程设计需求. 本文发展了一种保持组件顺序的特征驱动结构拓扑优化方法. 首先提出了基于杆链的设计变量设置方案, 将当前杆的终点设置为下一杆的起点, 以此获得特定组件顺序的结构构型. 其次提出了打印路径的总长度约束, 以精确地控制原材料的消耗; 提出了相邻杆之间的夹角约束, 以避免在3D打印路径的转角处出现尖锐的角度. 此外考虑了组件之间的非独立关系, 对相关解析函数的灵敏度进行分析. 最后, 通过数值算例验证了该方法对于保持组件顺序结构设计的有效性和优越性.